Energy Storage Materials 74 (2025) 103975

Contents lists available at ScienceDirect

Energy Storage Materials

journal homepage: www.elsevier.com/locate/ensm

Improving the rate performance of lithium metal anodes: In-situ formation of 3D interface structures by mechanical mixing with sodium metal

Markus Mann [a], Christian Schwab [a], Lara Caroline Pereira dos Santos [b], Robert Spatschek [b], Dina Fattakhova-Rohlfing [a,c,*], Martin Finsterbusch [a,d,*]

[a] Institute of Energy Materials and Devices: Materials Synthesis and Processing (IMD-2) Forschungszentrum Jülich GmbH, Wilhelm-Johnen-Straße, 52425 Jülich, Germany
[b] Institute of Energy Materials and Devices: Structure and Function of Materials (IMD-1) Forschungszentrum Jülich GmbH, Wilhelm-Johnen-Straße, 52425 Jülich, Germany
[c] University Duisburg-Essen, Faculty of Engineering and Center for Nanointegration Duisburg-Essen CENIDE, Lotharstraße 1, 47057 Duisburg, Germany
[d] Helmholtz Institute Münster: Ionics in Energy Storage (IMD-4), Forschungszentrum Jülich GmbH, Wilhelm-Johnen-Straße, 52425 Jülich, Germany

ARTICLE INFO

Keywords:
Lithium metal anodes
Lithium sodium eutectic
Critical current densities
LLZO
Solid state electrolytes

ABSTRACT

Lithium metal anodes (LMA) increase the energy density of lithium-ion batteries, but the formation of lithium dendrites above a critical charging current (CCD) is still a severe safety issue that limits their wide industrial application. In this work, we present a simple, scalable method to improve the properties of LMA and increase the CCD by physical mixing with a small amount of Na metal, leading to a formation of self-organized 3D interfacial structures during cycling. The physical premixing of Li and Na metal results in excellent dispersion of the metals without phase separation or clustering. To demonstrate the effectiveness of these LiNa anodes in solid-state cells with oxide-ceramic $Li_{6.45}Al_{0.05}La_3Zr_{1.6}Ta_{0.4}O_{12}$ (LLZO) separators, we melt-quench them directly onto the LLZO surface. The application of a special formation protocol during cycling leads to the in-situ formation of a 3D Na-metal interfacial structure, which improves the cell performance. The symmetric cells prepared in this way were operated without external pressure (0.1 MPa) and showed record CCDs for planar interfaces of over 5.0 mA•cm^{-2}, cycling stability of over 1200 cycles, and a total stripping capability of up to 100 μm Li metal, corresponding to a capacity of 21 mAh•cm^{-2}. Most remarkably, our approach resulted in a very low impedance of the Li/LLZO interface, which remained constant even at high stripping/plating rates. The new approach provides an industrially scalable method for fabricating next generation LMAs with an inherently reduced tendency to dendrite formation, which can be readily utilized in a variety of next-generation lithium batteries.

1. Introduction

To increase the energy density of current Li-ion batteries (LIBs), the use of lithium metal anodes (LMA) with its extremely high gravimetric capacity of 3860 mAh•g^{-1} instead of currently used graphite- or graphite/Si anode materials is highly desirable. To date, reversible stripping and plating of lithium during battery cycling has been a challenge, especially for conventional liquid electrolyte LIBs, as lithium does not plate uniformly and forms mossy/dendritic lithium that can short-circuit the cell, leading to thermal runaway, venting, and subsequent cell fire [1,2]. To counteract this failure, solid-state electrolytes such as Li-ion conducting polymers (e.g., polyethylene oxide, PEO) have been extensively studied as they were believed to be resistant to dendrite growth due to their high mechanical strength. However, dendrites were also observed in polymer electrolytes, and Li-metal anodes remained unattainable.

Monroe and Newman developed a model for dendrite growth and found that it could be successfully suppressed when the shear modulus of the solid electrolyte was at least twice the lithium modulus (4.8 GPa at 298 K) [3]. While most polymeric electrolytes cannot meet this criterion at suitable ionic conductivity [4–6], the discovery of the oxide solid electrolyte $Li_7La_3Zr_2O_{12}$ (LLZO) was a turning point. LLZO combines high total ionic conductivity at room temperature (RT) with chemical stability to Li metal and has a remarkably high shear modulus above 50 GPa and elastic modulus above 100 GPa [7–12]. Surprisingly, Ishiguro et al. found that even LLZO exhibits dendritic Li metal growth when a

* Corresponding authors.
E-mail addresses: d.fattakhova@fz-juelich.de (D. Fattakhova-Rohlfing), m.finsterbusch@fz-juelich.de (M. Finsterbusch).

https://doi.org/10.1016/j.ensm.2024.103975
Received 14 October 2024; Received in revised form 9 December 2024; Accepted 18 December 2024
Available online 19 December 2024

certain critical current density (CCD) is exceeded [13]. In recent years, many studies have attempted to elucidate the underlying mechanisms of dendrite growth in LLZO, and several causes of dendritic Li growth have been found, depending on the properties of the sample. Since oxide solid electrolytes are mostly polycrystalline, the grain boundaries and pores in their microstructure have been identified as pathways for dendrite growth [14,15]. However, it has also been shown that dendrite growth in single crystalline LLZO occurs at a CCD below 1 mA•cm^{-2} when surface defects are present, making the fracture toughness K_{Ic} another critical factor for dendrite resistance [16–18]. Moreover, the contact between LLZO and Li metal has been found to have a great influence on the CCD. Above a certain current density, the lithium atoms that are removed from the interface during stripping cannot be replenished from the bulk of the LMA to a sufficient extent [19–22]. This effect leads to void formation, which break the contact at the interface between solid electrolyte and anode, and results in a greatly increased effective current density at the remaining point contacts, so that the effective current density exceeds the stability of the material and dendrites are formed.

The main reason for the formation of voids at the rigid LLZO/Li interface is the low self-diffusion coefficient of the Li metal, which describes the mobility of Li atoms in the metal either by plastic deformation or by chemical diffusivity. To overcome this limitation, considerable efforts have been made to increase the diffusivity by alloying lithium with various elements such as Al [23], Ag [24], Au [25,26], Cu_6Sn_5 [27], Ge [28], Mg [29,30], Si [31] or Sn [27,32]. Although higher self-diffusion coefficients have been demonstrated for several compositions and low interfacial resistances have been achieved, the alloy typically changes the ductility of the LMA. High ductility can be important as increasing the cell pressure during operation is another approach to obtain good contact between the lithium metal anode and the separator. Sufficient pressure plastically deforms the lithium metal and leads to a collapse of possible voids formed at the interface [19,30], but since competitive batteries require very thin LLZO separators (e.g., free-standing separators produced by tape casting) that can break at high pressure, the applicability of this method for practical batteries is limited. A more universal approach is to increase the effective contact area [17] by three-dimensional anode concepts such as porous LLZO anode support structures [33–35], metal sponges [36–38] or carbon nanotube-infused Li, which are able to deliver sufficient capacities and current densities [34,39]. However, while some approaches reduce the effective energy density quite dramatically, their manufacturing is quite complex and the problem of contact loss is not completely eliminated. Therefore, a facile and industrial scalable method to fabricate LMAs with a lower risk of dendrite formation through the in-situ formation of a 3D interface structure would be a breakthrough for commercialization.

In the approach presented here, we use small amounts of Na mechanically mixed into the Li metal (LiNa) prior to anode fabrication to create such 3D interlayers that form in-situ during the formation cycles.

A look at the equilibrium phase diagram shows that lithium and sodium are miscible only in narrow concentration ranges of the liquid state and are phase separated in the solid state [40]. Theoretically, a fine rod-like microstructure of dispersed lithium and sodium metals could form when the liquid monotectic composition is quenched, leading to the in-situ formation of a 3D sodium scaffold in lithium matrix. However, such a 3D structure has never been reported, and usually the mixing of Na and Li in the liquid phase leads to phase separation with the formation of large clusters of individual metals. Even without a finely dispersed structure, the addition of 0.5 wt% to 47.42 wt% sodium to the molten lithium has been shown to be beneficial for anode performance, as it reacts with impurities such as Li_2CO_3 at the LLZO surface and reduces the interfacial resistance [41,42].

The combination of the surface-cleaning properties of the Na metal with the formation of a 3D Na substructure in the Li anode is expected to further improve cell performance. However, quenching a monotectic LiNa melt on a current collector or a ceramic separator does not seem feasible on an industrial scale, mainly because it does not lead to the formation of a 3D architecture. One possible reason for this could be that the two phases segregate during slow cooling, which makes the large-scale production of the finely dispersed LiNa anodes from the molten state an additional challenge. Furthermore, this process requires extremely dry and oxygen-free atmosphere, as the molten metals react very quickly with traces of O_2 and H_2O.

In this work, we have found a way to overcome the challenges described above and produce LiNa anodes with improved performance. A key step in this process is the physical premixing of Li and Na by repeated folding, resulting in LiNa anode foils with excellent dispersion of the metals without phase separation or clustering. Physical mixing at room temperature reduces the amount of unwanted reaction products compared to the molten state, as the reaction with atmospheric impurities is slower. By heating the LiNa foils on the LLZO separator at 300 °C and subsequent quenching, we were not only able to achieve excellent contact between anode and solid electrolyte, but also suppress sodium segregation, which is still extremely well dispersed in the Li matrix. After the formation cycles, our anodes showed for the first time an in-situ formed 3D interfacial layer that maintains a permanent contact between the LLZO separator and the LiNa anode, thus enabling high capacity cycling. Due to the immiscibility of Li and Na in the solid state, the formed 3D structure is also very stable during cycling and can withstand over 1000 cycles.

2. Results and discussion

Sodium is much softer than lithium and could reduce the hardness of a mixed LiNa foil, promoting the plastic deformation leading to the collapse of voids at the interface. However, lithium and sodium are virtually immiscible over the entire composition range, with an eutectic point occurring near the sodium-rich end at 3 mol% Li (eutectic temperature 92 °C) and a monotectic point on the lithium-rich side at 97 mol % Li (monotectic temperature 170 °C) [40]. The monotectic composition was chosen for the preparation of Li-Na (LiNa) anode foils in this work. In order to achieve a good distribution of Na in the Li host structure, physical mixing was chosen over in-melt mixing, as the latter usually leads to segregation of Na in large clusters (demixing), especially in the region of mutual immiscibility of Li- and Na-rich melt phases. During mechanical mixing, Li and Na metal were weight in the desired amounts, mixed and calendered to obtain a thin, flat foil of roughly combined metals. This foil was then cut into multiple pieces, folded and calendered to the same thickness as before. This process was repeated at least 20 times to ensure a homogeneously, finely dispersed Na in Li metal which could then be applied to the LLZO pellets (Fig. 1).

Since mechanical treatment often increases the hardness of the metal foils (work hardening) [43], which would mitigate the desired metal softening, we performed a detailed mechanical characterization of selected samples to evaluate the effect of the processing steps and composition on the mechanical properties of the anodes. As a reference sample (Foil 1), we used a pure Li metal foil that was mechanically rolled from Li pellets and calendered. The sample labeled Foil 2 was a pure Li metal foil that was mechanically folded and calendered 20 times. For the sample labeled Foil 3, we used the same fabrication process as for Foil 2, but with the mechanical mixture of 3 mol% Na and 97 mol% Li metal. The sample labeled as Foil 4 is the LiNa anode after melt bonding. For that, Foil 4 was heated at 300 °C for 5 min between two Ni foils and quenched on a metallic surface in the glovebox, following therefore the same procedure as the symmetric cell preparation explained in the methods section.

The Martens hardness measured on the differently processed foils clearly shows a work hardening effect induced by the mechanical treatment, which leads to an increase in hardness of up to 19 % after multiple calendering steps (Fig. 2a). The addition of 3 mol% Na has only a very small effect, leading to a slight increase in hardness compared to similarly treated Li foil. Melt-quenching of the LiNa foil leads to a slight reduction in hardness, which however remains approx. 17 % higher than

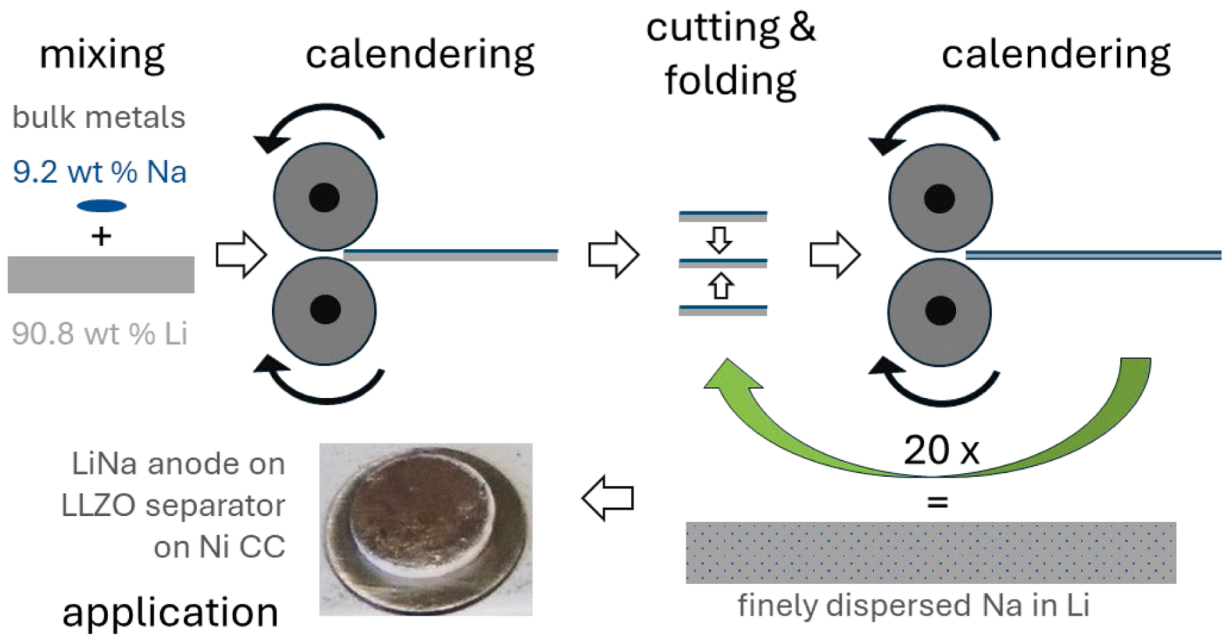

Fig. 1. Manufacturing process of the LiNa anode: 1) mechanical mixing of stoichiometric amounts of lithium and sodium metal, 2) first calendering to obtain a foil, 3) cutting and folding, and 4) repeated calendering. Steps 3 and 4 are repeated at least 20 times, resulting in a fine distribution of sodium in lithium. The finished foil is then attached to the LLZO separator (inset) for electrochemical testing.

the pure Li foil. This effect was attributed to a strong crystalline texturing of the LiNa foil during mechanical mixing. After mixing, a preferred 100 orientation was observed, which was randomized again during heat treatment (Fig. 2b–f). Since Na addition did not lead to the softening of the metal anode, all performance improvements shown in the later sections were not caused by plastic deformation, i.e. collapse of voids forming at the interface, thus allowing low or even pressureless operation of practical cells with such anodes.

To fabricate the symmetric cells for electrochemical characterization, the freshly calendered LiNa foils were pressed by hand onto both sides of a LLZO pellet and sandwiched between two nickel current collectors. To achieve good interfacial contact between the metal electrode and LLZO and to regain the BCC lattice of the two alkali metals, the cell was then heated to 300 °C for five minutes and immediately quenched to room temperature on a metal plate (See Fig. 1, application). To investigate the distribution of Li and Na in such an electrode, the Foil 4 prepared in the same way was cross-cut with a plasma focused ion beam (plasma FIB) and analyzed using scanning electron microscopy (SEM). The SEM images with backscattered and secondary electrons (Fig. S1) show a homogeneous contrast with no signs of demixing and phase separation, indicating that a monotectic solid solution was formed after electrode fabrication.

Low interfacial resistance between solid electrolyte and metal anode is one of the key properties of a cell, which has a decisive effect on its performance. Electrochemical impedance spectroscopy (EIS) measurements show that the interfacial resistance of the cells with LiNa anodes is exceptionally low, even without any adhesion layers or LLZO surface modification, and is below 2 $\Omega \bullet cm^{-1}$ (Fig. S2). This value is in line with the best LLZO|Li interface resistances reported in literature [19,41, 44–47].

The critical current density (CCD), *i.e.*, the current density at which a short circuit of the cell occurs, is another key property used to characterize dendrite tolerance of cells. To determine the CCD, we used an established protocol that is widely accepted for the study of cells with Li metal anodes. For this purpose, the current density was applied in 100 incremental steps from 0.05 to 5.0 $mA \bullet cm^{-2}$ and the cell voltage was measured. The measurement was stopped when the polarization reached the stop criterion of 1.0 V, indicating almost complete contact loss, or when a voltage drop indicated the onset of dendrite growth, taking the current at which this occurred as the CCD.

At 60 °C, the symmetric reference cell with pure lithium electrodes showed an overpotential of −44.5 mV at 2.2 $mA \bullet cm^{-2}$ during the third plating cycle, and the polarization increased sharply until it reached −1.0 V (>20 times the starting voltage). During this increase, a voltage drop was also measured, which is a clear sign of the onset of dendrite formation. Therefore, the reference CCD is 2.2 $mA \bullet cm^{-2}$ for pure Li anodes (Fig. S3).

In contrast to pure Li, the cell with LiNa electrodes showed lower polarization. Even at the highest applied current density of 5.0 $mA \bullet cm^{-2}$ and after 300 stripping/plating cycles, no dendrite formation was observed and the potential increased only 2.4-fold (from −102 mV to −240 mV), well below the stopping criterion of 1.0 V (Fig. 3a). Therefore, the CCD of at least 5.0 $mA \bullet cm^{-2}$ at 60 °C was determined for LiNa electrode cells, which already meets the critical milestones for high energy and high power solid-state batteries [48].

The change in electrode polarization agrees well with the evolution of the interfacial resistance with varying current density as determined by EIS (Fig. 3b). In contrast to the reference cells with pure Li electrodes, where the interfacial resistance typically increases with increasing polarization current, the cells with LiNa electrodes show an opposing trend. In fact, all contributions to the cell impedance decrease with repeating cycling, after an initial small increase at low polarization currents up to 1.0 $mA \bullet cm^{-2}$. At first, the bulk and GB contributions appear to increase by about 2 %, only to drop again as the interface resistance stabilizes at its very low values. The origin of this effect is not entirely clear, as it is not observed in the other cells that cycle with constant current densities. However, the very slight deviation of 2 % is within the scatter of the values over the different current densities, which is much greater than the given standard deviation of the individual fittings (error bars on each data point). Nevertheless, it is noteworthy that even at high polarization currents, the interfacial resistance remains virtually constant during several hundred stripping/plating cycles (Fig. 3c), which distinguishes our electrode from all LLZO|Li cells reported so far. Similar to the cells with pure Li electrodes, the initial increase in interface impedance of cells with LiNa electrodes can be explained by the decrease in contact area due to stripping of lithium

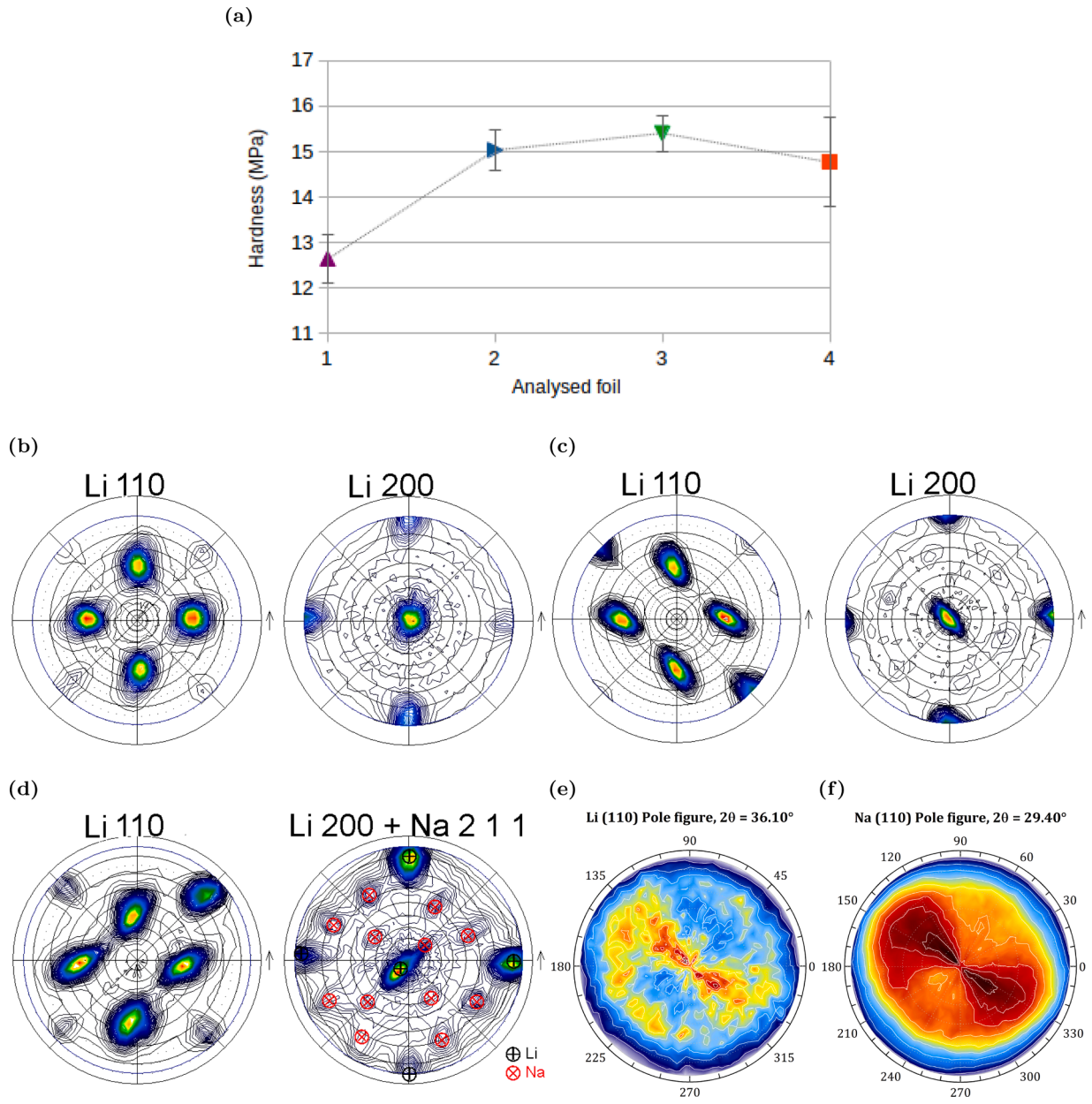

Fig. 2. Martens hardness (a) and pole figures (b-f) of Li and LiNa foils after different fabrication steps. Foil 1 is pure untreated Li metal foil, Foil 2 is pure Li metal foil which was mechanically treated, Foil 3 is a LiNa foil before heat treatment, and Foil 4 is the LiNa foil after the heat treatment. Average and standard deviation are taken from 130 indents. Experimental set up at $\boldsymbol{F} = 15\ \boldsymbol{mN}/10\boldsymbol{s}$. Pole figures for Foil 1 (b), Foil 2 (c) and Foil 3 (d) show a strong 100 single-crystal-like texture, indicating that the calendering procedure generates the 100 preferred orientation. The measurements on Foil 4 (e and f) show no preferred orientation, confirming that the heat treatment erases the texture. (e) is the reflection from Li (110), while (f) is the reflection from Na (110). Due to overlapping reflections with the Ni foil, some pole figures (e.g., Li (200)) cannot be measured for Foil 4.

with formation of voids.

However, the subsequent decrease in resistance is observed for LiNa electrodes only and is therefore likely due to the presence of Na metal, as will be discussed later. Since cycling with low currents up to 1.0 $mA{\bullet}cm^{-2}$ was found to decrease the LiNa|LLZO interfacial resistance, this procedure was used in further experiments as formation cycles for all cells tested.

In comparison, measurements at 25 °C also showed improvements in CCD, which reached 1.15 $mA{\bullet}cm^{-2}$. Due to the lower temperature, the resistance associated with the bulk and grain boundaries of the LLZO increases by a factor of ~4.5 compared to 60 °C, which is due to the lower ionic conductivity of LLZO at this temperature. Interestingly, the interface resistance increases by a factor of 50 for the first cycle and drops to a factor of 20 in the subsequent cycles (Fig. S4). While the interfacial resistance remains constant at a low level, the difference in temperature dependence indicates that the activation energy of Li transfer at the interface is higher than for bulk and GB conductivity, which could be related to contact geometry resistance of the system, with its activation energy increasing due to current constriction [19]. Further experiments with different Na contents and formations cycles, coupled with in situ analysis of the 3D Na structure, could elucidate the exact nature of this effect more precisely.

The exceptionally high interfacial stability of cells with LiNa electrodes is also evident in long-term galvanostatic stripping/plating experiments, which are used to characterize the cycling stability of the batteries and are particularly important for practical application. In these measurements, the same amount of Li metal (determined electrochemically as the amount of charge transferred in each cycle and

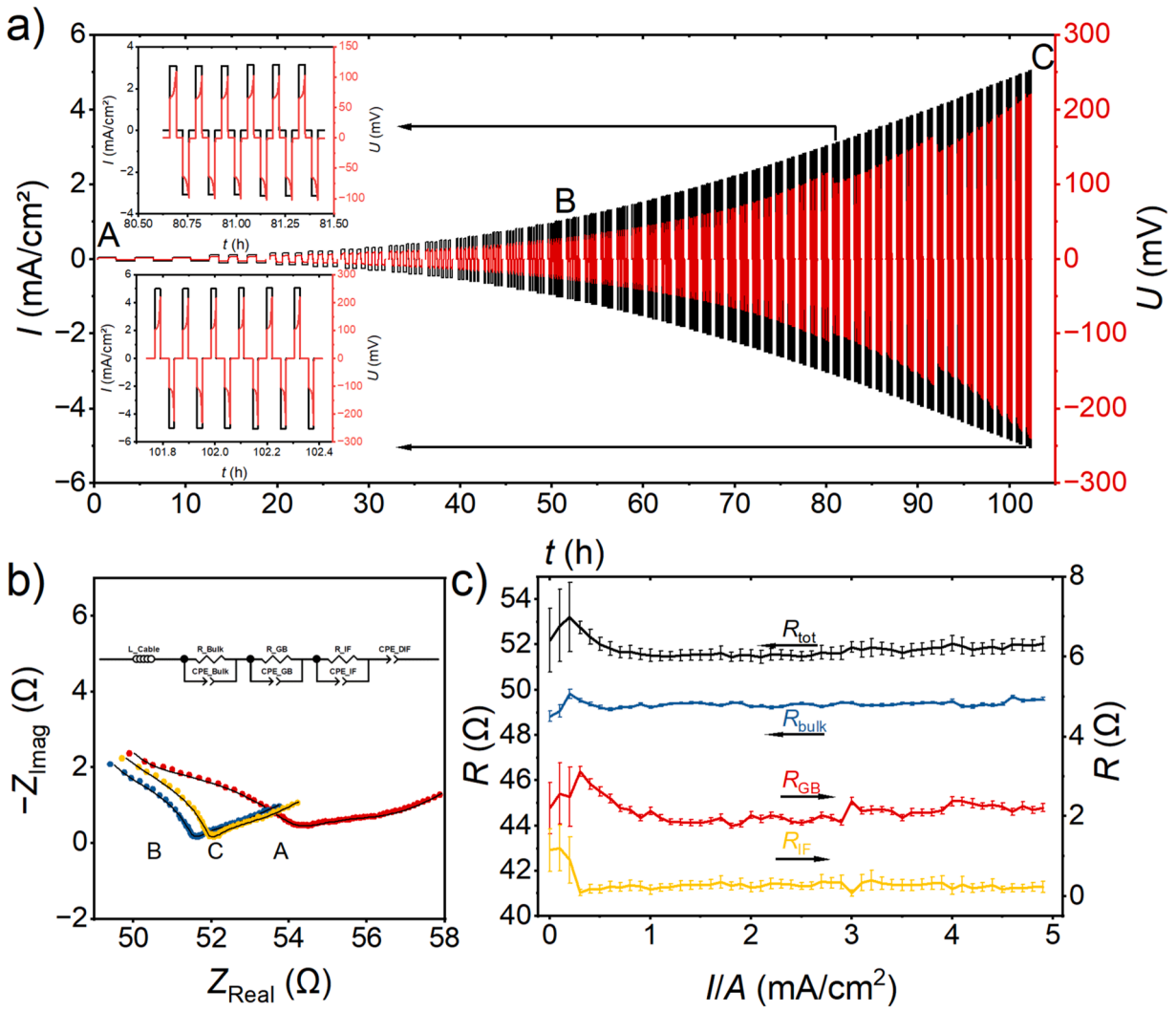

Fig. 3. a) CCD measurement on a symmetric LiNa|LLZO|LiNa cell at 60 °C. Black and red lines indicate applied current density and change in cell polarization, respectively. b) Nyquist plots of the impedance spectra for the cell shown in the Fig. 3a, recorded after different electrochemical treatments: A, freshly assembled cell (red), B, after CCD test up to 1.0 mA•cm^{-2} (blue) and C, after CCD test at 5.0 mA•cm^{-2} (yellow). Equivalent circuit is shown in the inset. c) Evolution of the different contributions to the total impedance during CCD measurements of the cell in Fig. 3a, obtained by fitting the impedance spectra in Fig. 3b: total resistance (R_{tot}) in black, bulk resistance (R_{bulk}) in blue, grain boundary (R_{GB}) resistance in red and interface resistance (R_{IF}) in yellow.

fixed at 0.1 mAh•cm^{-2}) was transferred between the electrodes at different rates and repeated 200 times at each current density (Fig. 4a). It is noticeable that the cell has a very low total impedance of about 54 Ω, which practically does not change even at a current density of 3.0 mA•cm^{-2}. Moreover, all contributions to the total impedance, including the LiNa|LLZO interface resistance, remain virtually the same after 300 cycles during CCD tests and another 900 cycles during long-term measurements. Only at the highest applied current density of 3.0 mA•cm^{-2} a slight decrease in bulk (R_{bulk}) and grain boundary (R_{GB}) resistance is observed, which could be interpreted as the onset of dendrite formation (Fig. 4). However, the absolute resistance decrease is very small at 2.8 Ω and 0.6 Ω for bulk and grain boundary resistance, respectively, so the amount of dendrites is likely to be negligible but could increase with increasing capacity.

To investigate how much capacity can be plated at a given current density, long-term stripping and plating experiments were performed. In literature, the total amount of Li that can be stripped and plated with pure lithium anodes is usually limited to 1–2 mAh•cm^{-2} at a current density of 0.1 mA•cm^{-2} at 25 °C [19,21,39]. For our experimental setup, similar results were obtained, with a total amount of 1 mAh/cm^2 at 0.5 mA/cm^2 and 5 mAh/cm^2 at 0.1 mA/cm^2 at 60 °C (Fig. S5). In all cases, pure Li-metal 2D anodes with non-optimized interfaces lead to an increase in interfacial resistance, ultimately resulting in dendrite formation when larger amounts of Li are stripped/plated.

Such an increase in interfacial resistance was not observed in our electrodes, even in cells already exposed to the CCD measurement protocol. Therefore, we investigated the total amount of Li that can be stripped and plated using a cell that was preconditioned up to 1.0 mA•cm^{-2} by a CCD test procedure and thus already exhibited the lowest interface resistance. In contrast to the literature, our modified anode allowed a total stripping capacity of 11.5 mAh•cm^{-2} at 25 °C at 0.1 mA•cm^{-2} and still 5.1 mAh•cm^{-2} at 0.2 mA•cm^{-2}, which is an order of magnitude increase in available lithium compared to the pure metal anode (Table 1). These values are also well above the typical requirements of commercial cells in terms of total capacity.

Since all-solid-state batteries can operate at elevated temperatures, we tested the total available capacity at 60 °C. During galvanostatic charging with a current density of 0.2 mA•cm^{-2}, two potential plateaus were observed before the total available lithium was stripped (Fig. 5). The first plateau is observed when stripping up to 6 mAh•cm^{-2} lithium, which corresponds to a Li layer thickness of about 30 μm. This process can therefore be attributed to the stripping of Li metal in close proximity

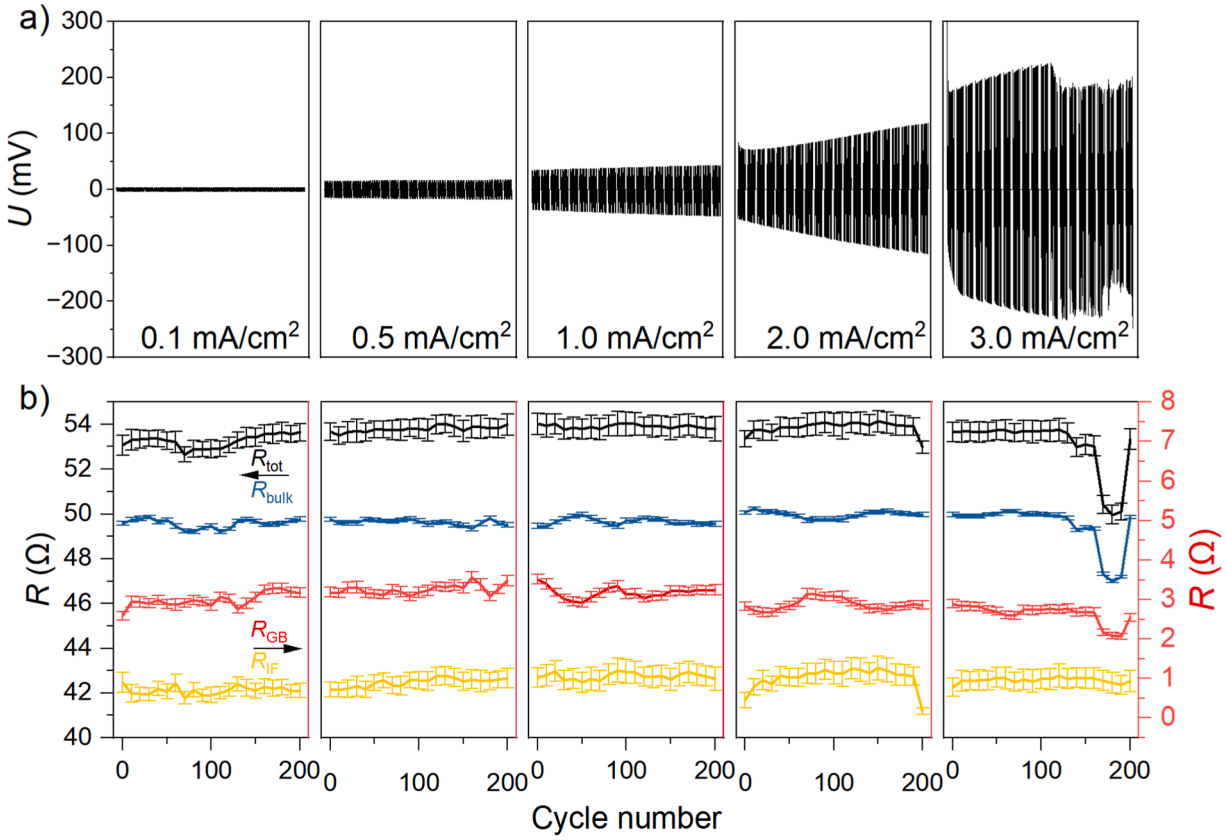

Fig. 4. a) Voltage profile of a symmetric LiNa|LLZO|LiNa cell at 60 °C during galvanostatic stripping and plating of the same amount of Li metal (0.1 mAh•cm^{-2}) at current densities of 0.1 mA•cm^{-2}, 0.5 mA•cm^{-2}, 1.0 mA•cm^{-2}, 2.0 mA•cm^{-2}, and 3.0 mA•cm^{-2}. Cells were cycled 200 times at each current density. b) Evolution of the different contributions to the total impedance during galvanostatic cycling of the cell in Fig. 2a, obtained by fitting the impedance spectra using the equivalent circuit shown in Fig. 1b: total resistance (R_{tot}) in black, bulk resistance (R_{bulk}) in blue, grain boundary (R_{GB}) resistance in red and interfacial resistance (R_{IF}) in yellow. Impedance spectra were recorded after every ten cycles.

Table 1
Measured capacities from total stripping experiments of LiNa anodes performed at different temperatures and current densities. Note that the total electrode thickness/capacity of the 25 °C sample was about half that of the 60 °C sample.

Temp. (°C)	*I/A (mA•cm^{-2})*	*Stripped Cap. (mAh•cm^{-2})*	*Stripped Li (μm)*	*D_{eff} (cm^2•s^{-1})*
25	0.1	11.527	56.0	9.7(2)•10^{-11}
25	0.2	5.121	24.9	8.6(1)•10^{-11}
60	0.2	21.590	104.8	3.64(4)•10^{-10}
60	0.5	14.127	68.6	5.95(4)•10^{-10}
60	1.0	7.129	34.6	6.00(3)•10^{-10}

to the LLZO surface, which is consistent with the estimate of available lithium capacity reported in the literature [19,21,39]. The second plateau corresponds to the removal of an additional 15.6 mAh•cm^{-2} of lithium. In total, 21.6 mAh•cm^{-2} at 0.2 mA•cm^{-2} was available for stripping, which means that almost 105 μm of dense Li was completely transferred to the other side of the symmetric cell. This value is approximately equal to a thickness of our anode layer, leaving the anode side virtually lithium-free. The second plateau can therefore be attributed to the transport of lithium in the bulk of the metal foil, *i.e.*, inside the LiNa microstructure. A similar behavior has already been observed by Fuchs et al. for lithium infused with carbon nanotubes [39], however, an increase in interfacial polarization was observed for their samples, resulting in a much lower CCD compared to this study. In our case, the rapid increase in polarization is due to Li depletion of the anode as all available Li is stripped.

To understand this outstanding performance, which is due to only small additions of sodium, it is worthwhile to take a closer look at the polarization behavior. To this end, the EIS spectra were measured periodically (voltage dips in Fig. 5a) at open circuit potential (OCV), *i.e.*, without polarization of the sample. The interfacial resistance R_{IF} between LLZO and LiNa anode remains almost constant during the stripping experiments (Fig. 5b), which gives clear evidence that an intimate contact between LLZO surface and bulk lithium is maintained by our modified electrode. While the bulk resistance R_{Bulk} and grain boundary resistance R_{GB} in LLZO remain virtually constant, a slight increase in impedance can be seen on the low frequency side of the spectrum. From the capacities extracted from the EIS fit, we can assign the semicircle at low frequency to unknown diffusion processes, however, the overall increase is also small and cannot explain the sharp increase in polarization observed in Fig. S6.

Thus, we conclude that the 3D Na metal scaffold structure provides sufficient interfacial contact even when the anode is completely stripped of Li. This structure is able to distribute electrons and lithium ions evenly and serves as a nucleation site for lithium metal deposition.

Since our cell operates without applied external pressure (only about 1 atm ambient pressure on the cell) and thus mechanical deformation of lithium to improve the interface can be ruled out, Li diffusion within the metal anode is a rate-limiting step. To compare our samples, we calculated the effective diffusion coefficient D_{eff} using Sand's equation (SI Eqs. (1-5) [49]. At 25 °C, D_{eff} reaches a value of ~1•10^{-10} cm^2•s^{-1}, which is twice the values of 5.1•10^{-11} cm^2•s^{-1} and 2.3•10^{-11} cm^2•s^{-1}

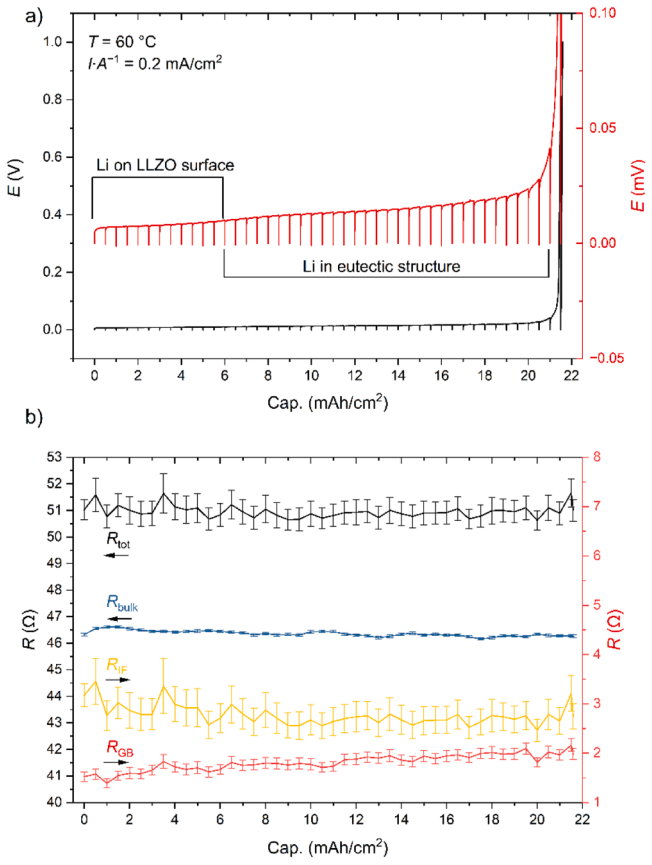

Fig. 5. a) Voltage profile of a symmetric LiNa|LLZO|LiNa cell at 60 °C during galvanostatic stripping at a current density of 0.2 mA•cm^{-2}. The voltage range up to 1.0 V is shown in black and the magnification of the same graph in red. b) Evolution of the different contributions to the total impedance during the stripping experiment of the cell in Fig. 5a, obtained by fitting the impedance spectra partially shown in Fig. S6.

reported in the literature for pure lithium [22] or a Li-Mg alloy [30], respectively. At 60 °C and low current density, the effective diffusion coefficient is about 3.6•10^{-10} cm^2•s^{-1} and the anode is completely stripped of lithium, limiting the capacity. A similar behavior has been observed before under similar conditions in the literature (50 °C, $I/A \leq$ 0.25 mA•cm^{-2} [22,25]), but could not been explained at the mechanistic level. At higher current densities, we apparently reach the diffusion limit at about ~6•10^{-10} cm^2•s^{-1}, where lithium is only partially stripped from the anode. In this range, the extractable capacity depends on the current density and remains at about ~7 mAh•cm^{-2} at 1.0 mA•cm^{-2} at 60 °C for stripping. This is additional evidence of the superior lithium mobility in our 3D LiNa microstructure and highlights the potential advantages of this electrode morphology.

Since lithium metal adheres very strongly to the LLZO surface, the lithium layer generally cannot be removed from the LLZO separator. However, since the lithium could be completely extracted from our LiNa electrode during galvanostatic stripping, we were able to easily detach it from the separator and examine the morphology using scanning electrode microscopy (SEM). As expected, it was found that the surface of the LLZO separator was completely covered by a porous sodium layer, although no sodium was intentionally deposited (Fig. 6a and b). Therefore, it can be assumed that this sodium layer formed during the initial cycling from the evenly distributed Na in the LiNa foil, which was melted and quenched on the LLZO pellet during cell assembly. The presence of the Na layer can explain the very low interfacial resistance of our cells, since Na reacts with any resistive impurities on the LLZO surface such as lithium oxides or carbonates. Moreover, Na remains electrochemically inert at the potentials applied during electrochemical cycling but provides electronic conductivity, which is why the sodium layer can provide a morphologically stable electrical contact between the LLZO pellet and the metal anode.

This hypothesis is confirmed by post-mortem analysis of the surface of the nickel current collector, which could be separated from the LLZO pellet because it no longer contained lithium after complete Li stripping. The analysis showed that it was completely covered by a uniform layer of highly porous sodium (Fig. 6c and d). This shows that the sodium layer forms a coherent 3D scaffold that bridges the LLZO and the Ni current collector after complete removal of Li and has a sponge-like morphology with a disordered but uniform porosity with a pore size of about 20–50 μm. This structure increases the effective surface area of the electrode, provides electrical contact, faster surface diffusion, and thus enables higher available capacities compared to a dense 2D lithium morphology. EDX spectra of the Na-covered LLZO and current collector confirm the presence of sodium and can be found in the supporting information (Figs. S7 and S8).

We demonstrated that the LLZO with LiNa electrode can sustain current densities of 5.0 mA•cm^{-2} and 2.0 mA•cm^{-2} for short and long cycle times, respectively. This result is among the highest for CCDs in general and is the highest at 60 °C (Table 2).

The most likely mechanism leading to this champion performance is outlined in Fig. 7. The unique approach to preparing the monotectic mixture of 5 vol% Na in Li results in a finely distributed Na metal phase in Li, even after the melt-quenching. Fig. 7a sketches such a finely dispersed structure of Na (blue) in a Li (grey) metal anode, the polycrystalline LLZO in yellow below, and the Ni current collector in orange on top. Upon polarization (Fig. 7b), Li is stripped from the interface and forms voids due to the limited self-diffusion of bulk Li. However, the voids favor faster Li diffusion at their internal surface [19], and in addition, the Na deposits as larger inclusions (blue particles) at the interface, also promoting Li diffusion (Red arrows in Fig. 7b). The overall thickness of the electrode will shrink, leading more and more Na being “plated” at the LLZO interface. If Li is partially stripped during these formation cycles, an intermediate state between B and C will form. In the extreme case, when all Li is removed (Fig. 7c), the porous 3D Na structure observed in the SEM still provides electrical contact between the Ni current collector and the LLZO surface. This structure leads to the improved and constant interfacial resistance and enables high CCDs. During the subsequent plating (Fig. 7d), the diffusion within the 3D Na metal is faster than in the Li bulk (short red arrow in Fig. 7d), but it was shown that the available capacity for high current densities is still limited by the bulk diffusion (long red arrow in Fig. 7d). Therefore, additional strategies to improve bulk transport would further increase the available capacities of Li metal anodes and make them attractive not only for solid-state batteries, but especially for batteries with a first discharge cycle such as Li-S, or batteries featuring a conversion type cathode.

3. Conclusion

By physically mixing Li and Na metals at room temperature in a ratio close to the monotectic composition, a fine dispersion of the elements can be achieved without phase separation. While cycling such a LiNa anode, a 3D interfacial structure is formed in-situ, which improves the performance in terms of CCD, cycling stability and total plating capacity even in cells with planar interfaces and no external pressure application.

As proof of concept, symmetric cells were fabricated by direct melt-quenching of the LiNa foils on the planar surface of LLZO pellets used as separator. Due to the 3D Na-metal interface structure, these cells were able to withstand record current densities of 5.0 mA•cm^{-2} during incremental testing without external pressure, which is one of the critical milestones for industrial application [48]. In long term-cycling tests, the CCD was still higher than 2.0 mA•cm^{-2} after 800 cycles, and the interfacial impedance between LiNa-anode and LLZO separator

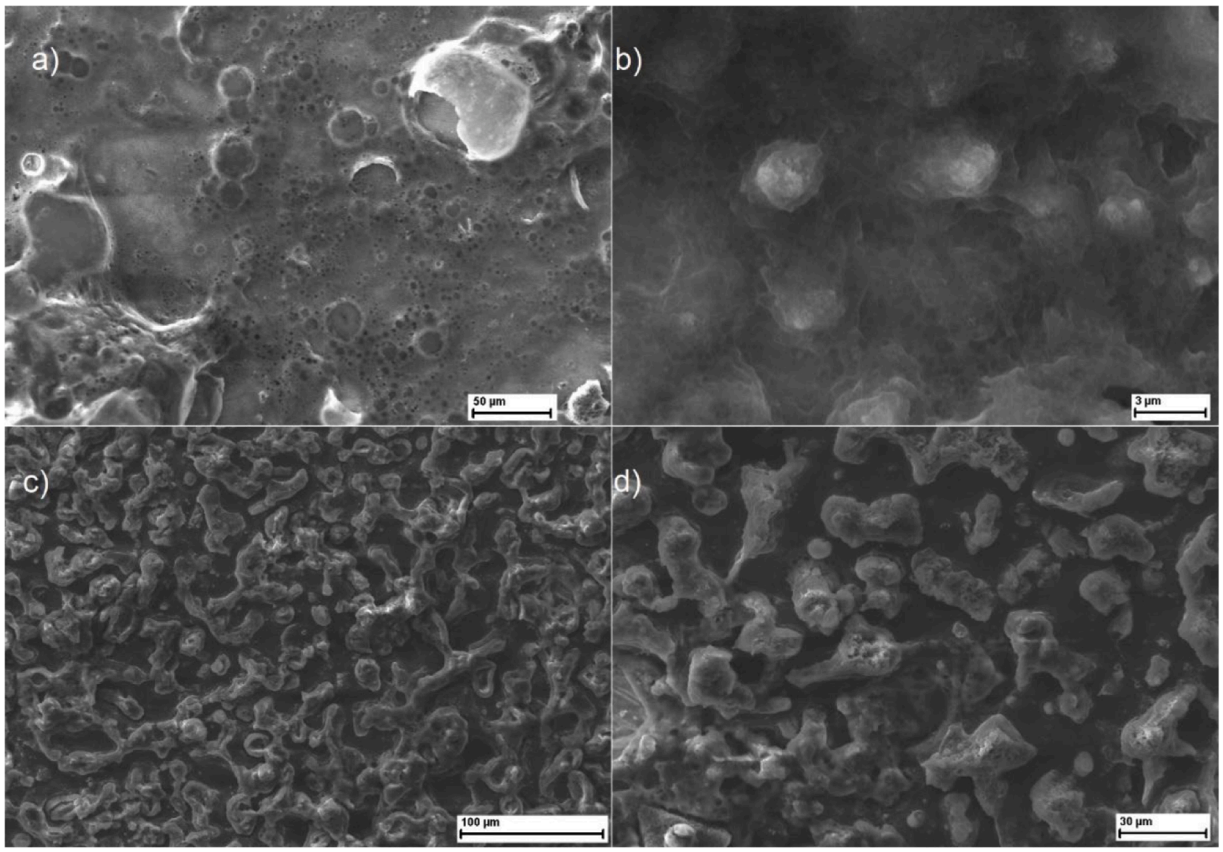

Fig. 6. (a, b) SEM images at different magnification of the LLZO surface after a symmetrical cell was fully polarized (Li completely stripped). The surface is almost fully covered by sodium. (c, d) SEM images at different magnification of the Ni current collector surface after lithium was fully stripped. The surface is covered by a sodium scaffold.

Table 2
Reported critical current densities (CCD) of different LLZO with different modifications, measured at different temperatures and current densities.

LLZO	Modification	Condition	CCD ($mA \bullet cm^{-2}$)	Ref.
$Li_{6.76}Al_{0.24}La_3Zr_2O_{12}$	Li_3BO_3	25 °C	0.35	[50]
$Li_{6.4}La_3Zr_{1.4}Ta_{0.6}O_{12}$	$InCl_3$	RT	0.7	[51]
$Li_{6.45}Al_{0.05}La_3Zr_{1.6}Ta_{0.4}O_{12}$	–	60 °C	0.35	[47]
$Li_{6.45}Al_{0.05}La_3Zr_{1.6}Ta_{0.4}O_{12}$	$LiNbO_3$	60 °C	>0.45	[47]
$Li_{6.5}La_3Zr_{1.5}Ta_{0.5}O_{12}$	Zn:Cu	28 °C	2.8	[52]
$Li_{6.4}Ga_{0.2}La_3Zr_2O_{12}$	Single crystal	20 °C	0.28	[17]
$Li_{6.25}Al_{0.25}La_3Zr_2O_{12}$	-	25 °C	0.93	[53]
$Li_{6.25}Al_{0.25}La_3Zr_2O_{12}$	-	40 °C	1.48	[53]
$Li_{6.25}Al_{0.25}La_3Zr_2O_{12}$	-	60 °C	2.57	[53]
$Li_{6.25}Al_{0.25}La_3Zr_2O_{12}$	-	80 °C	4.07	[53]
$Li_{6.25}Al_{0.25}La_3Zr_2O_{12}$	-	100 °C	6.70	[53]
$Li_{6.5}La_3Zr_{1.5}Ta_{0.5}O_{12}$	Li-CNT	25 °C, 3.4 MPa	0.6	[39]
$Li_{6.5}La_3Zr_{1.5}Ta_{0.5}O_{12}$	HCl	25 °C	1.6	[54]
$Li_{6.5}La_3Zr_{1.5}Ta_{0.5}O_{12}$	HCl	60 °C	2.6	[54]
$Li_7La_3Zr_2O_{12}$	-	30 °C, 2 MPa	0.6–0.7	[55]
$Li_{6.5}La_3Zr_{1.5}Ta_{0.5}O_{12}$	-	30 °C, 7 MPa	1.4–1.5	[55]
$Li_{6.5}La_3Zr_{1.5}Ta_{0.5}O_{12}$	–	195 °C	530(140)	[56]
$Li_{6.4}La_3Zr_{1.4}Ta_{0.6}O_{12}$	LiNa	RT	>1.5	[41]
$Li_{6.5}La_3Zr_{1.5}Ta_{0.5}O_{12}$	LiNa	RT	1.1	[42]
$Li_{6.5}La_3Zr_{1.5}Ta_{0.5}O_{12}$	LiNa	60 °C	3.7	[42]
$Li_{6.45}Al_{0.05}La_3Zr_{1.6}Ta_{0.4}O_{12}$	–	60 °C	2.2	This work
$Li_{6.45}Al_{0.05}La_3Zr_{1.6}Ta_{0.4}O_{12}$	LiNa	60 °C	>5.0	This work

remained low. Finally, the monotectic LiNa anode achieved remarkable capacities at 25 °C and 60 °C in full-stripping experiments, reaching cycled capacities of 21 $mAh \bullet cm^{-2}$, which correspond to ~100 µm of pure Li metal. The calculated effective diffusion coefficient D_{eff} was twice as high compared to pure lithium, reaching $\sim 1 \bullet 10^{-10}$ $cm^2 \bullet s^{-1}$ at 25 °C. At 60 °C, the diffusion limit of D_{eff} $\sim 6.0 \bullet 10^{-10}$ $cm^2 \bullet s^{-1}$ was reached.

This overall increase in performance in combination with higher stability and the simple manufacturing process can bring advanced lithium-metal anodes closer to industrial application, especially in combination with solid separators.

4. Experimental section/methods

4.1. Preparation of LiNa electrodes

To avoid demixing of Li and Na during cooling, we physically mixed stoichiometric amounts of lithium (99.99 %, Alfa Aesar) and sodium (99.8 %, Alfa Aesar) rather than melting them together. In this process, we calendered the metals into foils and folded the foils. This was repeated at least 20 times until a homogeneous distribution was achieved. A mixture of Li with 3 mol% (5.36 vol%, 9.29 wt%) Na was chosen since this composition has a monotectic point at ~170 °C [40].

4.2. Preparation of LLZO symmetric cells

$Li_{6.45}Al_{0.05}La_3Zr_{1.6}Ta_{0.4}O_{12}$ was prepared by solid-state reaction. The starting materials $LiOH \bullet H_2O$ (AppliChem, 99 %), La_2O_3 (Merck, 99.9 %, 10 h pre-dried at 900 °C), ZrO_2 (Treibacher, 99.5 %), Ta_2O_5 (Treibacher, 99.99 %) and Al_2O_3 (Inframat, 99.9 %) were mixed in an intensive mixer

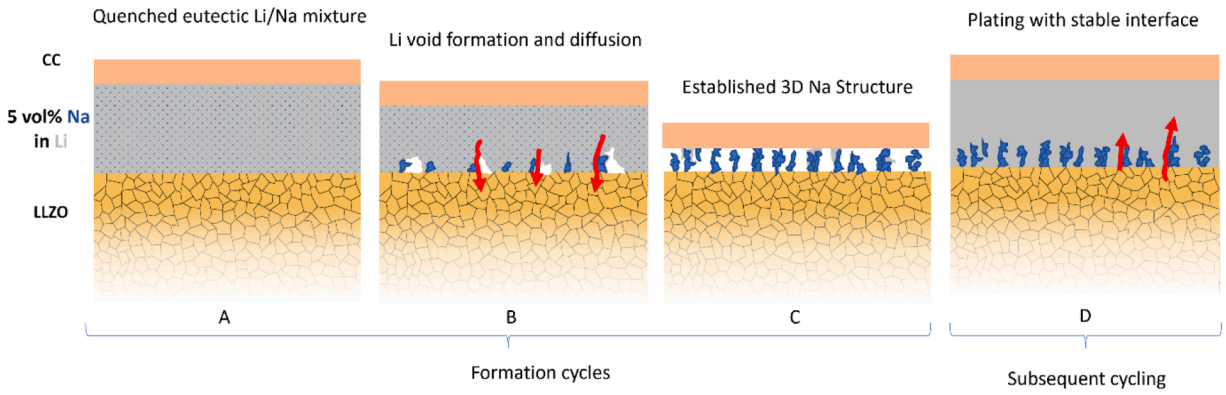

Fig. 7. Schematic of the formation mechanism of the 3D Na interface structure, starting with the monotectic mixture after quenching (A), Li migration through the bulk and along void surfaces (red arrows) accompanied by consolidation of the metal electrode during stripping (B), the fully established 3D Na structure in the Li depleted state after high-capacity stripping (C) and the most likely metal electrode structure upon replating of the full Li capacity (D).

(EIRICH laboratory mixer type EL1), pressed into pellets and calcined at 850 °C for 20 h in a high temperature muffle furnace (Nabertherm GmbH, Lilienthal, Germany) in an aluminum oxide crucible. The calcined powder was ground with an electrical mortar grinder (RM 200, Retsch GmbH, Haan, Germany) with a tungsten-carbide crucible and calcined for a second time at 1000 °C for 20 h. The final LLZO powder was pressed into the pellets and sintered in a closed alumina crucible at 1175 °C in air for 10 h in the high-temperature muffle furnace. The sintered pellets had a diameter of ~7 mm. XRD shows pure cubic LLZO phase. The crystallographic density of ρ(XRD) = 5.348 g•cm^{-3} was determined by Rietveld refinement using the Fullprof program package [57]. The refinement can be found in the supporting information (Fig. S9). On average, the pellets had a geometric density of ρ(geo) = 5.31(3) g•cm^{-3}, which corresponds to a relative density of 99.3(7)%. The pellets were cut into 0.7 mm thick slices with a diamond saw (Iso-Met, Buehler, ITW Test & Measurement GmbH, Leinfelden-Echterdingen, Germany) and were manually pre-polished in ambient atmosphere. The separators were then transferred into a glove box. For the fabrication of symmetric cells, both sides of the LLZO separators were manually polished using SiC sandpaper with an 800 grit. Metal electrodes were then plated manually by pressing freshly calendered foils onto the fresh polished separators. The symmetrical cell was placed between two nickel current collectors and heated to 300 °C for five minutes. The hot cell was then quenched by placing it on a metal plate at ambient temperature. After cooling down to room temperature, the symmetrical cell was transferred into a Swagelok cell, sealed, and taken out of the glove box for analysis.

4.3. Investigation of hardness

Martens hardness of 100 μm thick pure lithium and LiNa foils are experimentally determined using micro-indentation. All experiments and sample preparation are conducted in an argon filled glove-box, in which oxygen and water content are kept below 0.1 ppm. The experiments are performed using a Fischerscope H100 indenter (Helmut Fischer GmbH, Sindelfingen, Germany) equipped with a diamond Vickers tip. Square samples are cut by a sharp blade from the original foil. The squared samples are attached to a metal sample holder, to provide support and stability during indentation. All measurements are performed at room temperature. The indentation experiments are load-controlled. The load is applied following $\frac{d\sqrt{F}}{dt}$, with loading and unloading at the same rate. After optimization, the experimental settings are fixed as F = 15 mN/10s. 130 indents are performed, from which average and standard deviation are calculated. The individual measurements are carried out with a space of at least 10 times the indentation depth in between each indent.

Additionally, XRD, texture and pole figure analyses are carried out on all specimens. These experiments are performed using a dome airtight sample holder, a diffractometer EMPYREAN (PANalytical) and Cu-K_α radiation.

4.4. Sample characterization

X-ray diffraction (XRD) analysis was performed using an Empyrean diffractometer (Malvern Panalytical GmbH, Kassel, Germany) with Cu-Kα radiation. The diffractometer was equipped with a PIXcel^{3D} area detector. The XRDs were measured in reflection geometry from 10 to 140° 2θ with a step size of 0.026°. Rietveld refinement of the XRD patterns was performed using the Fullprof package.

Scanning electron microscope (SEM) images were taken on a Zeiss EVO 15 (Carl Zeiss AG, Oberkochen, Germany) with an acceleration voltage of 15 kV. Energy-dispersive X-ray (EDX) spectra were measured using an Ultim Max 100 detector and analyzed using the AZtec software package (both Oxford Instruments plc, England).

Cross sections of LiNa between two Nickel foils were cut with a Xe-Plasma-FIB equipped on a Helios 5 Laser PFIB system (Thermo Fisher Scientific) and SEM images taken.

The electrochemical characterization was performed using a Bio-Logic VMP-300 multipotentiostat (Bio-Logic Sciences Instruments Ltd, Claix, France) and a VT 4002EMC climate chamber (Vötsch Industrietechnik GmbH, Balingen, Germany). Impedance spectra were measured at 25 °C with the program EC-Lab [58] at frequencies between 7 MHz to 1 Hz with an electrical field perturbation of 10 mV•mm^{-1}. The measured impedance spectra were fitted with RelaxIS3 (rhd instruments GmbH & Co, KG, Darmstadt, Germany) in the frequency range of 3.49 MHz to 1 Hz and 2.77 MHz to 5 Hz at 25 °C and 60 °C, respectively. The impedance spectra were fitted with an induction element L, three *R*-CPE elements and one final CPE-element. The induction element L_{Cable} was necessary because of the measurement setup and corresponds to the inductivity of the used cables. In order to assign the *R*-CPE elements to the corresponding physical counterparts, the effective capacitance *C* was calculated from the fitted resistance *R*, CPE coefficient *Q*, and the exponential parameter α (Eq. (1)) [59,60].

$$C = \frac{(Q \cdot R)^{\frac{1}{\alpha}}}{R} \tag{1}$$

Capacitances fit quite well to the reported values for bulk (10^{-11} F), grain boundaries (GB, 10^{-8} F) of an ion conductor, and as well as the interface resistance (IF, 10^{-5} F) between electrolyte and electrode [61].

To determine the critical current density (CCD) for lithium dendrite formation, lithium stripping and plating experiments were performed using BioLogic VMP-300 multipotentiostat. Cells were heated to 60 °C and capacity-controlled galvanostatic cycling was performed at 0.1 mAh•cm^{-2} starting at 50 μA•cm^{-2} and increasing by 50 μA•cm^{-2} per

cycle. Every 30 s, a data point was recorded. Additional data points were recorded if the measured voltage showed a deviation of >10 mV from the previous data point to detect micro short-circuits. Additionally, after every 0.1 mA•cm^{-2} stripping and plating increment, impedance spectra were measured. Total stripping experiments were performed with symmetrical cells at different current densities (0.1 – 1.0 mA•cm^{-2}) and temperatures (25 °C and 60 °C). The cells were polarized until the stopping criterion of 1.0 V was reached. An impedance spectrum was measured every 0.5 mAh•cm^{-2}.

CRediT authorship contribution statement

Markus Mann: Writing – original draft, Visualization, Investigation, Conceptualization. **Christian Schwab:** Writing – review & editing, Visualization, Investigation. **Lara Caroline Pereira dos Santos:** Writing – review & editing, Visualization, Investigation. **Robert Spatschek:** Writing – review & editing, Supervision, Funding acquisition. **Dina Fattakhova-Rohlfing:** Writing – review & editing, Writing – original draft, Supervision, Funding acquisition, Conceptualization. **Martin Finsterbusch:** Writing – review & editing, Writing – original draft, Visualization, Supervision, Funding acquisition, Conceptualization.

Declaration of competing interest

The authors declare the following financial interests/personal relationships which may be considered as potential competing interests:

D. Fattakhova-Rohlfing reports financial support was provided by German Federal Ministry of Education and Research (BMBF). Dina Fattakhova-Rohlfing reports a relationship with Federal Ministry of Education and Research Bonn Office that includes: funding grants. If there are other authors, they declare that they have no known competing financial interests or personal relationships that could have appeared to influence the work reported in this paper.

Acknowledgments

This work was part of the project ALANO supported by German Federal Ministry of Education and Research (BMBF). Financial support from the BMBF under grant numbers 03XP0396D (ALANO), 13XP0510A (CatSE^2), 13XP0434A (FestBatt 2-Oxid), and 13XP0258B (Meet Hi-End III) is gratefully acknowledged. The authors thank Philipp Hecker (IMD-2) and Grit Häuschen (IMD-2) for the synthesis of LLZO pellets and Mirko Ziegner (IMD-1) for the XRD analyses of the Li and LiNa foils.

Supplementary materials

Supplementary material associated with this article can be found, in the online version, at doi:10.1016/j.ensm.2024.103975.

References

[1] K. Nishikawa, T. Mori, T. Nishida, Y. Fukunaka, M. Rosso, T. Homma, In Situ Observation of Dendrite Growth of Electrodeposited Li Metal, J. Electrochem. Soc. 157 (11) (2010), https://doi.org/10.1149/1.3486468.

[2] M. Nojabaee, D. Kopljar, N. Wagner, K.A. Friedrich, Understanding the nature of solid-electrolyte interphase on lithium metal in liquid electrolytes: a review on growth, properties, and application-related challenges, Batter. Supercaps 4 (6) (2021) 909–922, https://doi.org/10.1002/batt.202000258.

[3] C. Monroe, J. Newman, The impact of elastic deformation on deposition kinetics at lithium/polymer interfaces, J. Electrochem. Soc. 152 (2) (2005), https://doi.org/10.1149/1.1850854.

[4] J. Fan, C.A. Angell, The preparation, conductivity, viscosity and mechanical properties of polymer electrolytes and new hybrid ionic rubber electrolytes, Electrochim. Acta 40 (13–14) (1995) 2397–2400, https://doi.org/10.1016/0013-4686(95)00202-p.

[5] G. Nikolakakou, C. Pantazidis, G. Sakellariou, E. Glynos, Ion conductivity–shear modulus relationship of single-ion solid polymer electrolytes composed of polyanionic miktoarm star copolymers, Macromolecules 55 (14) (2022) 6131–6139, https://doi.org/10.1021/acs.macromol.2c00620.

[6] S.H. Kim, J.K. Choi, Y.C. Bae, Mechanical properties and ionic conductivity of gel polymer electrolyte based on poly(vinylidene-fluoride-co-hexafluoropropylene), J. Appl. Polym. Sci. 81 (4) (2001) 948–956, https://doi.org/10.1002/app.1516.

[7] S. Yu, et al., Elastic properties of the solid electrolyte $Li_7La_3Zr_2O_{12}$ (LLZO), Chem. Mater. 28 (1) (2015) 197–206, https://doi.org/10.1021/acs.chemmater.5b03854.

[8] J.E. Ni, E.D. Case, J.S. Sakamoto, E. Rangasamy, J.B. Wolfenstine, Room temperature elastic moduli and Vickers hardness of hot-pressed LLZO cubic garnet, J. Mater. Sci. 47 (23) (2012) 7978–7985, https://doi.org/10.1007/s10853-012-6687-5.

[9] J. Wolfenstine, J.L. Allen, J. Sakamoto, D.J. Siegel, H. Choe, Mechanical behavior of Li-ion-conducting crystalline oxide-based solid electrolytes: a brief review, Ion. (Kiel) 24 (5) (2017) 1271–1276, https://doi.org/10.1007/s11581-017-2314-4.

[10] G. Yan, J.F. Nonemacher, H. Zheng, M. Finsterbusch, J. Malzbender, M. Krüger, An investigation on strength distribution, subcritical crack growth and lifetime of the lithium-ion conductor $Li_7La_3Zr_2O_{12}$, J. Mater. Sci. 54 (7) (2019) 5671–5681, https://doi.org/10.1007/s10853-018-03251-4.

[11] A.-N. Wang, J.F. Nonemacher, G. Yan, M. Finsterbusch, J. Malzbender, M. Krüger, Mechanical properties of the solid electrolyte Al-substituted $Li_7La_3Zr_2O_{12}$ (LLZO) by utilizing micro-pillar indentation splitting test, J. Eur. Ceram. Soc. 38 (9) (2018) 3201–3209, https://doi.org/10.1016/j.jeurceramsoc.2018.02.032.

[12] J.F. Nonemacher, Y. Arinicheva, G. Yan, M. Finsterbusch, M. Krüger, J. Malzbender, Fracture toughness of single grains and polycrystalline $Li_7La_3Zr_2O_{12}$ electrolyte material based on a pillar splitting method, J. Eur. Ceram. Soc. 40 (8) (2020) 3057–3064, https://doi.org/10.1016/j.jeurceramsoc.2020.03.028.

[13] K. Ishiguro, et al., Ta-doped $Li_7La_3Zr_2O_{12}$ for water-stable lithium electrode of lithium-air batteries, J. Electrochem. Soc. 161 (5) (2014) A668–A674, https://doi.org/10.1149/2.013405jes.

[14] E. Milan, M. Pasta, The role of grain boundaries in solid-state Li-metal batteries, Mater. Future. 2 (1) (2022), https://doi.org/10.1088/2752-5724/aca703.

[15] S. Patra, J. Narayanasamy, T. Panneerselvam, R. Murugan, Review—microstructural modification in lithium garnet solid-state electrolytes: emerging trends," (in English), J. Electrochem. Soc. 169 (3) (Mar 1 2022), https://doi.org/10.1149/1945-7111/ac5c99.

[16] K. Kataoka, H. Nagata, J. Akimoto, Lithium-ion conducting oxide single crystal as solid electrolyte for advanced lithium battery application, Sci. Rep. 8 (1) (2018) 9965, https://doi.org/10.1038/s41598-018-27851-x.

[17] F. Flatscher, M. Philipp, S. Ganschow, H.M.R. Wilkening, D. Rettenwander, The natural critical current density limit for Li7La3Zr2O12 garnets, J. Mater. Chem. A 8 (31) (2020) 15782–15788, https://doi.org/10.1039/c9ta14177d.

[18] L. Porz, et al., Mechanism of lithium metal penetration through inorganic solid electrolytes, Adv. Energy Mater. 7 (20) (2017), https://doi.org/10.1002/aenm.201701003.

[19] T. Krauskopf, H. Hartmann, W.G. Zeier, J. Janek, Toward a fundamental understanding of the lithium metal anode in solid-state batteries-an electrochemo-mechanical study on the garnet-type solid electrolyte $Li_{6.25}Al_{0.25}La_3Zr_2O_{12}$, ACS Appl. Mater. Interface. 11 (15) (Apr 17 2019) 14463–14477, https://doi.org/10.1021/acsami.9b02537.

[20] T. Krauskopf, F.H. Richter, W.G. Zeier, J. Janek, Physicochemical concepts of the lithium metal anode in solid-state batteries, Chem. Rev. 120 (15) (Aug 12 2020) 7745–7794, https://doi.org/10.1021/acs.chemrev.0c00431.

[21] T. Krauskopf, B. Mogwitz, H. Hartmann, D.K. Singh, W.G. Zeier, J. Janek, The fast charge transfer kinetics of the lithium metal anode on the garnet-type solid electrolyte $Li_{6.25}Al_{0.25}La_3Zr_2O_{12}$, Adv. Energy Mater. 10 (27) (2020), https://doi.org/10.1002/aenm.202000945.

[22] C.-L. Tsai, et al., Dendrite-tolerant all-solid-state sodium batteries and an important mechanism of metal self-diffusion, J. Power Source. 476 (2020), https://doi.org/10.1016/j.jpowsour.2020.228666.

[23] K.K. Fu, et al., Toward garnet electrolyte-based Li metal batteries: an ultrathin, highly effective, artificial solid-state electrolyte/metallic Li interface, Sci. Adv. 3 (4) (Apr 2017) e1601659, https://doi.org/10.1126/sciadv.1601659.

[24] W. Feng, X. Dong, P. Li, Y. Wang, Y. Xia, Interfacial modification of Li/Garnet electrolyte by a lithiophilic and breathing interlayer, J. Power Source. 419 (2019) 91–98, https://doi.org/10.1016/j.jpowsour.2019.02.066.

[25] C.-L. Tsai, et al., $Li_7La_3Zr_2O_{12}$ interface modification for Li dendrite prevention, ACS Appl. Mater. Interface. 8 (16) (Apr 27 2016) 10617–10626, https://doi.org/10.1021/acsami.6b00831.

[26] G.V. Alexander, S. Patra, S.V. Sobhan Raj, M.K. Sugumar, M.M. Ud Din, R. Murugan, Electrodes-electrolyte interfacial engineering for realizing room temperature lithium metal battery based on garnet structured solid fast Li^+ conductors, J. Power Source. 396 (2018) 764–773, https://doi.org/10.1016/j.jpowsour.2018.06.096.

[27] W. Feng, et al., Building an interfacial framework:Li/Garnet interface stabilization through a Cu_6Sn_5 layer, ACS Energy Lett. 4 (7) (2019) 1725–1731, https://doi.org/10.1021/acsenergylett.9b01158.

[28] W. Luo, et al., Reducing interfacial resistance between garnet-structured solid-state electrolyte and Li-metal anode by a germanium layer, Adv. Mater. 29 (22) (Jun 2017), https://doi.org/10.1002/adma.201606042.

[29] K.K. Fu, et al., Transient behavior of the metal interface in lithium metal-garnet batteries, Angew. Chem. Int. Ed. Engl. 56 (47) (Nov 20 2017) 14942–14947, https://doi.org/10.1002/anie.201708637.

[30] T. Krauskopf, B. Mogwitz, C. Rosenbach, W.G. Zeier, J. Janek, Diffusion limitation of lithium metal and Li–Mg alloy anodes on LLZO type solid electrolytes as a function of temperature and pressure, Adv. Energy Mater. 9 (44) (2019), https://doi.org/10.1002/aenm.201902568.

[31] W. Luo, et al., Transition from superlithiophobicity to superlithiophilicity of garnet solid-state electrolyte, J. Am. Chem. Soc. 138 (37) (Sep 21 2016) 12258–12262, https://doi.org/10.1021/jacs.6b06777.
[32] M. He, Z. Cui, C. Chen, Y. Li, X. Guo, Formation of self-limited, stable and conductive interfaces between garnet electrolytes and lithium anodes for reversible lithium cycling in solid-state batteries, J. Mater. Chem. A 6 (24) (2018) 11463–11470, https://doi.org/10.1039/c8ta02276c.
[33] C. Yang, et al., Continuous plating/stripping behavior of solid-state lithium metal anode in a 3D ion-conductive framework, Proc. Natl. Acad. Sci. U.S.A. 115 (15) (2018) 3770–3775, https://doi.org/10.1073/pnas.1719758115.
[34] S. Xu, et al., Three-dimensional, solid-state mixed electron-ion conductive framework for lithium metal anode, Nano. Lett. 18 (6) (2018) 3926–3933, https://doi.org/10.1021/acs.nanolett.8b01295.
[35] A. Neumann, et al., Effect of the 3D structure and grain boundaries on lithium transport in garnet solid electrolytes, ACS Appl. Energy Mater. 4 (5) (2021) 4786–4804, https://doi.org/10.1021/acsaem.1c00362.
[36] J. Yu, et al., Graphene-modified 3D copper foam current collector for dendrite-free lithium deposition, Front. Chem. 7 (2019) 748, https://doi.org/10.3389/fchem.2019.00748.
[37] J. Bao, et al., In situ formed synaptic Zn@LiZn host derived from ZnO nanofiber decorated Zn foam for dendrite-free lithium metal anode, Nano Res. (2022), https://doi.org/10.1007/s12274-022-5089-5.
[38] P. Li, et al., Anchoring an artificial solid-electrolyte interphase layer on a 3D current collector for high-performance lithium anodes, Angew. Chem. Int. Ed. Engl. 58 (7) (Feb 11 2019) 2093–2097, https://doi.org/10.1002/anie.201813905.
[39] T. Fuchs, et al., Increasing the pressure-free stripping capacity of the lithium metal anode in solid-state-batteries by carbon nanotubes, Adv. Energy Mater. (2022), https://doi.org/10.1002/aenm.202201125.
[40] M.G. Down, P. Hubberstey, R.J. Pulham, Sodium–lithium phase diagram: redetermination of the liquid immiscibility system by resistance measurement, J. Chem. Soc., Dalton Trans. (14) (1975), https://doi.org/10.1039/dt9750001490.
[41] X. Fu, et al., A high-performance carbonate-free lithium|garnet interface enabled by a trace amount of sodium, Adv. Mater. 32 (26) (Jul 2020) e2000575, https://doi.org/10.1002/adma.202000575.
[42] Y. Zhang, J. Meng, K. Chen, H. Wu, J. Hu, C. Li, Garnet-based solid-state lithium fluoride conversion batteries benefiting from eutectic interlayer of superior wettability, ACS Energy Lett. 5 (4) (2020) 1167–1176, https://doi.org/10.1021/acsenergylett.0c00383.
[43] B. Šesták, A. Seeger, The relationship between the work-hardening of B.C.C. and F.C.C. metals, Phys. Status Solid. 43 (1) (2006) 433–444, https://doi.org/10.1002/pssb.2220430146.
[44] L. Buannic, et al., Dual substitution strategy to enhance Li^+ ionic conductivity in $Li_7La_3Zr_2O_{12}$ solid electrolyte (in English), Chem. Mater. 29 (4) (2017) 1769–1778, https://doi.org/10.1021/acs.chemmater.6b05369, 2017/02/28.
[45] A. Sharafi, et al., Surface chemistry mechanism of ultra-low interfacial resistance in the solid-state electrolyte $Li_7La_3Zr_2O_{12}$, Chem. Mater. 29 (18) (2017) 7961–7968, https://doi.org/10.1021/acs.chemmater.7b03002.
[46] H. Zheng, et al., Intrinsic lithiophilicity of Li–garnet electrolytes enabling high-rate lithium cycling, Adv. Funct. Mater. 30 (6) (2019), https://doi.org/10.1002/adfm.201906189.
[47] M. Mann, et al., Anhydrous $LiNbO_3$ synthesis and its application for surface modification of garnet type Li-ion conductors, J. Electrochem. Soc. 169 (4) (2022), https://doi.org/10.1149/1945-7111/ac6836.
[48] S. Randau, et al., Benchmarking the performance of all-solid-state lithium batteries, Nat. Energy 5 (3) (2020) 259–270, https://doi.org/10.1038/s41560-020-0565-1, 2020/03/01.
[49] H.J.S. Sand, III. On the concentration at the electrodes in a solution, with special reference to the liberation of hydrogen by electrolysis of a mixture of copper sulphate and sulphuric acid, Lond. Edinb. Dublin Philos. Mag. J. Sci. 1 (1) (1901) 45–79, https://doi.org/10.1080/14786440109462590.
[50] T. Dussart, N. Rividi, M. Fialin, G. Toussaint, P. Stevens, C. Laberty-Robert, Critical current density limitation of LLZO solid electrolyte: microstructure vs interface, J. Electrochem. Soc. 168 (12) (2021), https://doi.org/10.1149/1945-7111/ac44be.
[51] J. Leng, et al., A facile and low-cost wet-chemistry artificial interface engineering for garnet-based solid-state Li metal batteries," (in English), Nano Energy 101 (2022), https://doi.org/10.1016/j.nanoen.2022.107603.
[52] X. He, et al., Cu-doped alloy layer guiding uniform Li deposition on a Li-LLZO interface under high current density, ACS Appl. Mater. Interface. 13 (35) (2021) 42212–42219, https://doi.org/10.1021/acsami.1c11607.
[53] M. Wang, J.B. Wolfenstine, J. Sakamoto, Temperature dependent flux balance of the $Li/Li_7La_3Zr_2O_{12}$ interface, Electrochim. Acta 296 (2019) 842–847, https://doi.org/10.1016/j.electacta.2018.11.034.
[54] S. Kim, et al., High-energy and durable lithium metal batteries using garnet-type solid electrolytes with tailored lithium-metal compatibility, Nat. Commun. 13 (1) (2022) 1883, https://doi.org/10.1038/s41467-022-29531-x.
[55] W. Chang, et al., Evolving contact mechanics and microstructure formation dynamics of the lithium metal-$Li_7La_3Zr_2O_{12}$ interface, Nat. Commun. 12 (1) (2021) 6369, https://doi.org/10.1038/s41467-021-26632-x.
[56] B. Kinzer, et al., Operando analysis of the molten Li|LLZO interface: understanding how the physical properties of Li affect the critical current density, Matter 4 (6) (2021) 1947–1961, https://doi.org/10.1016/j.matt.2021.04.016.
[57] J. Rodríguez-Carvajal, Recent advances in magnetic structure determination by neutron powder diffraction, Phys. B: Condens. Matter 192 (1–2) (1993) 55–69, https://doi.org/10.1016/0921-4526(93)90108-i, 1993/10/01/.
[58] EC-Lab, Bio-Logic - Science Instruments, 2021.
[59] M.E. Orazem, et al., Dielectric properties of materials showing constant-phase-element (CPE) impedance response, J. Electrochem. Soc. 160 (6) (2013) C215–C225, https://doi.org/10.1149/2.033306jes.
[60] C.H. Hsu, F. Mansfeld, Technical note: concerning the conversion of the constant phase element parameter Y_0 into a capacitance, Corrosion 57 (9) (2001) 747–748, https://doi.org/10.5006/1.3280607.
[61] J.T.S. Irvine, D.C. Sinclair, A.R. West, Electroceramics: characterization by impedance spectroscopy, Adv. Mater. 2 (3) (1990) 132–138, https://doi.org/10.1002/adma.19900020304.